Downlink ISAC with a Full-Stack 5G-Compliant Experimental Testbed: Communication vs. Control Signals for Multi-Target Detection

Salvatore Carbonara*†, Daniele Pugliese*†, Alessio Fascista*†, Angelo Coluccia‡†, Gennaro Boggia*†

*Dept. of Electrical and Information Engineering, Politecnico di Bari, Bari, Italy;
‡Department of Engineering, Università del Salento, Lecce, Italy;
†CNIT, Consorzio Nazionale Interuniversitario per le Telecomunicazioni.

***Abstract*—Integrated Sensing and Communication (ISAC) is envisioned as a key enabler for 5G and beyond mobile networks. While numerous theoretical works have demonstrated its potential, experimental studies employing 5G-compliant waveforms and full-stack implementations remain limited. In this work, we investigate monostatic downlink ISAC using a sub-6 GHz, full-stack, 5G-compliant experimental testbed built with software-defined radios, an advanced channel emulator, and the open source OpenAirInterface5G framework. We specifically compare the use of communication and control signals for multi-target detection. To this end, we develop a complete digital signal processing pipeline, encompassing the acquisition and temporal alignment of the TX/RX I/Q samples, followed by matched-filter or channel-estimation-like processing, and multi-target detection on the resulting range–Doppler maps. To mitigate the issue of erroneous multiple detections for a same dominant lobe, we propose a clustering strategy that effectively reduces false alarms while enhancing visibility of dominant targets. Experimental results reveal excellent sensing performance when communication signals are employed, owing to their larger bandwidth and longer transmission duration. Nevertheless, meaningful sensing is also obtained via control signals, which, despite their reduced information, have the notable advantage of continuous availability (always-on) even in the absence of active users.**

***Index Terms*—5G, Integrated Communication and Sensing, Software-Defined Radio, multi-target detection, Control Signals**

I. Introduction

ISAC has gained significant traction in 5G and beyond networks [1], where it is considered a key enabler for applications such as smart cities, autonomous driving, UAV detection, and remote healthcare [2]. Several studies have theoretically investigated ISAC approaches that reuse existing communication systems, e.g. [3]–[5], within the so-called *communication-centric design* [6]; however, experimentation remains challenging and often relies on simulated 5G-like waveforms. Focusing on monostatic ISAC, experimental evaluations employing mmWave transceivers and signals resembling the 5G radio frame have been presented in [7], [8]. The sub-6 GHz domain has been analyzed in [9], [10] using a synthetic OFDM waveform which, however, does not fall within the bandwidth and Subcarrier Spacing (SCS) parameters of 5G standards. In [11], a comprehensive analysis is presented about reusing 5G-compliant signals for sensing, also conducting an experimental campaign using synthetic waveforms. A preliminary study of monostatic ISAC over a full-stack 5G-compliant network is presented in [12], leveraging a digital processing with Self-Interference (SI) mitigation and shedding insights into the trade-offs in the range–Doppler maps related to residual interference and the use of 5G communication (payload traffic) signals. The use of control signals broadcast by the 5G Node B (gNB) — i.e., Synchronization Signal Block (SSB), COntrol REsourceSET (CORESET) #0, and System Information Block Type 1 (SIB1) — for sensing has been also considered. For instance, a study on the use of SSB and SIB1 is presented in [13]; nevertheless, the analyses are conducted in a simulated environment, using 5G-like waveforms. The adoption of control vs. payload signals entails a clear trade-off between ISAC continuity and performance. Indeed, control signals, which are always-on, occupy only a limited portion of time-frequency resources, typically around 10–15% in 5G New Radio (NR), so constraining the achievable sensing resolution and accuracy [6]. Conversely, data payloads represent 85% of time-frequency resources, so offering substantial improvements in range-Doppler resolution, target detection probability, and parameter estimation accuracy; still, communication signals are present only during periods of users activity, a bursty and application-dependent process that renders sensing availability inherently non-persistent and unpredictable.

This work focuses on monostatic ISAC using a full-stack, 5G-compliant experimental testbed built with software-defined radios (SDRs), an advanced channel emulator — which enables evaluation of sensing performance under complex scattering environments — and the OpenAirInterface5G (OAI) framework. We compare the use of full-band communication signals, generated during active downlink data transmission, with always-on control signals broadcast by the 5G network. While accumulation of information across multiple frames can be considered for improving the performance of control signals, this introduces additional latency and system complexity [6]; therefore, in this work we process only single radio frames, so representing a challenging scenario that, however, reveals the lower bound of practically achievable sensing performance. To this end, we develop a digital signal processing pipeline in which channel-estimation-like processing is applied to communication signals, while matched filtering is employed

for control signals. The resulting range–Doppler maps are processed through a multi-target detection algorithm, followed by a novel clustering strategy designed to suppress false alarms arising from multiple raw detections linked to a same dominant lobe in the range–Doppler map. Experimental results confirm that communication signals enable superior ISAC performance, but a single frame of control signals, though much less informative, still provides meaningful sensing information and allow for persistent ISAC operation even in the absence of active users.

II. 5G NR Physical Layer, Control and Communication Signals, and ISAC Processing

A. 5G NR Physical Layer and Always-on Signals

Let the 5G NR transmitted *resource grid*, before the Cyclic Prefix (CP) insertion, be $\boldsymbol{X} \in \mathbb{C}^{S\times M}$, where $m = 0,\dots,M-1$ and $s = 0,\dots,S-1$ denote the Orthogonal Frequency-Division Multiplexing (OFDM) symbols and subcarriers, respectively. This work is concerned with downlink ISAC through a full-stack standard-compliant gNB. Indeed, the transmitted signal $\boldsymbol{X}$ strictly adheres to the constraints imposed by the 5G, as it is generated by a real-world experimental testbed in which both the gNB and the User Equipment (UE) operate through a full protocol stack. Specifically, during the downlink periods, each element of $\boldsymbol{X}$ is allocated to transmit either Physical Downlink Shared Channel (PDSCH), Physical Downlink Control Channel (PDCCH), or SSB signals. When at least one user is connected to the gNB, the PDSCH portion conveys higher-layer data, whereas the PDCCH carries the control information required to maintain the connection. The frame portions carrying the PDCCH can be dynamically allocated and are referred to as CORESETs. Even when no UE is attached to the cell, the PDSCH, PDCCH, and SSB signals are still transmitted and can therefore be regarded as *always-on* signals.

Fig. 1 illustrates two time–frequency segments of a single radio frame with always-on signals (*TDA1* and *TDA5*) recorded by our experimental testbed in Sec. III. These are periodically transmitted, typically every 20 ms (depending on gNB configuration). The SSB occupies 20 Resource Blocks (RBs), corresponding to 240 subcarriers, and spans 4 OFDM symbols. Its frequency allocation depends on the NR band and SCS employed. During the attachment phase, the UE searches for the SSB as it carries synchronization signals, namely, the Primary Synchronization Signal (PSS) and Secondary Synchronization Signal (SSS), and the Physical Broadcast Channel (PBCH) containing the Master Information Block (MIB). Among other parameters, the MIB provides the position of CORESET #0 with respect to the SSB, corresponding to the first PDCCH frame portion. Within CORESET #0, additional parameters are conveyed through a Downlink Control Information (DCI) message, which is divided into Control Channel Elements (CCEs), each comprising 6 resource elements consisting of 1 RB (comprising in turn 12 subcarriers) and 1 OFDM symbol. The UE decodes these CCEs to locate its control information. From this, the time allocation within the PDSCH region and the size of the SIB1 can be derived. The SIB1 contains the

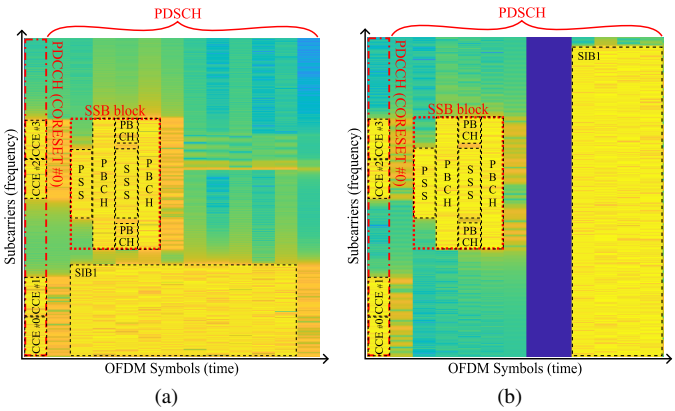

Fig. 1. Recorded always-on signals corresponding to (a) TDA1 and (b) TDA5.

remaining system configuration parameters that characterize the cell and enable the random access procedure. We focus on the analysis of the *TDA1* and *TDA5* since the location and size of both CORESET #0 and SIB1 depend on the specific configuration adopted. Specifically, the indices 1 and 5 correspond to the values defined in the 3GPP specifications that govern the time allocation of the SIB1. These two configurations were selected because in *TDA1* the SIB1 signal is predominantly distributed along the OFDM symbols, while in *TDA5* it mainly extends across the subcarriers — cf. Fig. 1(a) and (b) — so favoring Doppler resolution in the former case and range resolution in the latter case, as better discussed later.

B. ISAC Processing with Digital SI Mitigation

From the backscatter signal captured at the gNB RX channel, the received resource grid $\boldsymbol{Y} \in \mathbb{C}^{S\times M}$ is retrieved, whose (s,m)-th entry is the superposition of three components:

$$[\boldsymbol{Y}]_{s,m} = [\boldsymbol{Y}]^{\text{SI}}_{s,m} + \sum_{i=1}^{N_{\text{scat}}} \alpha_i [\boldsymbol{X}]_{s,m} e^{j2\pi(mT_{\text{symb}}f_i - s\Delta f \tau_i)} + w_{s,m},$$

where the first term is the undesired SI between the TX and RX channels, the second term N_{scat} dominant scatterers, and the third term additive noise. Each scatterer is characterized by its complex attenuation coefficient α_i, Doppler shift induced by relative movement f_i, and propagation delay τ_i, with Δf the SCS, T_{symb} the OFDM symbol duration.

From a communications standpoint, SI does not affect the performance of a Time Division Duplexing (TDD) system, since the RX signal is disregarded during data transmission. In contrast, during sensing, the RX signal carries echoes from surrounding objects that may be masked by residual SI, thereby hindering target detection. To mitigate this issue, we adopt the adaptive digital SI mitigation algorithm [14], with parameters tuned on our experimental setup (as discussed in [12]). The received resource grid after SI mitigation is denoted by $\tilde{\boldsymbol{Y}}$. By processing $\boldsymbol{X}$ and $\tilde{\boldsymbol{Y}}$ according to the monostatic ISAC paradigm [15], the Doppler shift and delay of the dominant scatterers can be estimated, and subsequently mapped to range and velocity information. We consider the following two alternative processing strategies, named *Matched Filter (MF)*

and *Channel Estimation-like (CH)* [11]. For the MF case, the RX and TX resource grids are elaborated as $\boldsymbol{F}^{\text{MF}} = \tilde{\boldsymbol{Y}} \odot \boldsymbol{X}^*$, with $\odot$ the Hadamard (element-wise) product and $(\cdot)^*$ the complex conjugate operator. In the CH case, the matrix is computed as $\boldsymbol{F}^{\text{CH}} = \tilde{\boldsymbol{Y}} \oslash \boldsymbol{X}$, with $\oslash$ the element-wise division.

Range and velocity can be estimated by analyzing the so-called radar image (or range–Doppler profile) obtained via the 2D periodogram, whose elements are computed as [16]

$$[\boldsymbol{P}]_{r,v} = \frac{1}{SM} \left| \sum_{s=0}^{\tilde{S}-1} \left(\sum_{m=0}^{\tilde{M}-1} [\boldsymbol{F}]_{s,m} e^{-j2\pi \frac{mv}{\tilde{M}}} \right) e^{j2\pi \frac{sr}{\tilde{S}}} \right|^2, \quad (1)$$

where $\tilde{M} \geq M$ and $\tilde{S} \geq S$ are set to be the size of the inner FFT (velocity profiles) and outer IFFT (range profiles), respectively, and $\boldsymbol{F}$ is computed as either $\boldsymbol{F}^{\text{MF}}$ or $\boldsymbol{F}^{\text{CH}}$. Furthermore, $v = -\tilde{M}/2, \ldots, \tilde{M}/2-1$ and $r = 0, \ldots, \tilde{S}-1$ indices the velocity and range bins, which can be mapped to the effective range and velocity values as

$$r_{\text{dist}} = cr/(2\tilde{S}\Delta f), \quad v_{\text{speed}} = cv/(2\tilde{M} T_{\text{symb}} f_{\text{carrier}}), \quad (2)$$

with c the speed of light, and f_{carrier} the carrier frequency.

C. Multi-target Detection Algorithm

Each cell (r, v) of the range-velocity map $\boldsymbol{P}$ is classified via a binary hypothesis test. Let $[\boldsymbol{P}]_{r,v}$ denote the detection statistic at range bin r and Doppler bin v, referred to as Cell Under Test (CUT); the decision rule is

$$[\boldsymbol{P}]_{r,v} \underset{H_0}{\overset{H_1}{\gtrless}} \eta, \quad (3)$$

where η represents the threshold, H_1 the hypothesis that the target is present in the CUT, and H_0 the null (target-free, noise-only) hypothesis. The value of η is set to guarantee a chosen probability of false alarm (P_{fa}). Specifically, we fix it over the entire periodogram $\boldsymbol{P}$, which can be expressed as:

$$P_{\text{fa}} = 1 - (1 - P_{\text{fa}}^{\text{CUT}})^{SM}, \quad (4)$$

where $P_{\text{fa}}^{\text{CUT}} = P(z > \eta | H_0)$ denotes the probability of false alarm at each CUT, readily computed as

$$P_{\text{fa}}^{\text{CUT}} = 1 - P(z \leq \eta | H_0) = 1 - F_z(\eta), \quad (5)$$

with z denoting the random amplitude of any bin in the periodogram $\boldsymbol{P}$ when H_0 is in force, and F_z the Cumulative Distribution Function (CDF) of the random variable z. Finally, substituting (5) into (4) and solving for η, we get

$$\eta = F_z^{-1}((1 - P_{\text{fa}})^{\frac{1}{SM}}), \quad (6)$$

If the additive noise samples $w_{s,m}$ are modeled as zero-mean complex Gaussian variables, the statistic z follows a chi-squared distribution. Accordingly, the threshold η would admit an explicit expression [17, Chapter 15]. Given the realistic experimental setup considered in this work, we instead adopt a distribution-agnostic approach and treat the distribution of z as unknown; accordingly, the CDF F_z (and thus its inverse) will be empirically estimated from the periodogram $\boldsymbol{P}$.

To deal with multiple and unknown number of targets N_{scat}, we employ a sequential detection-cancellation procedure. We begin by detecting the target corresponding to the largest peak in $\boldsymbol{P}$. Once the first target is identified, its contribution is removed from $\boldsymbol{P}$, and the detection test is repeated on the residual periodogram. This process continues until no CUT in the residual periodogram exceeds η, or when a predefined maximum number of iterations N_{it} is reached. The main steps of the algorithm are formalized as follows [18]:

1) Find $(\hat{r}, \hat{v}) = \arg\max_{r,v} [\boldsymbol{P}]_{r,v}^{(i)}$ (with $i = 0$ at the first iteration). If $[\boldsymbol{P}]_{\hat{r},\hat{v}}^{(i)} \leq \eta$, terminate;
2) add $(\hat{r}, \hat{v})$ to the list of targets, compute the associated range and velocity through (2), and then synthesize the single–target template $[\boldsymbol{F}]_{\hat{r},\hat{v}}$ (either MF or CH);
3) form the synthesized response $[\boldsymbol{F}]_{\hat{r},\hat{v}} e^{j2\pi(\frac{m\hat{v}}{\tilde{S}} - \frac{s\hat{r}}{\tilde{M}})}$ and compute its periodogram $[\boldsymbol{P}]_{\hat{r},\hat{v}}$ using (1);
4) subtract the periodogram of the single target $[\boldsymbol{P}]_{\hat{r},\hat{v}}$ from the current periodogram $[\boldsymbol{P}]_{r,v}^{(i)}$ and obtain the residual periodogram $[\boldsymbol{P}]_{r,v}^{(i+1)} = [\boldsymbol{P}]_{r,v}^{(i)} - [\boldsymbol{P}]_{\hat{r},\hat{v}}$;
5) Repeat from 1) until stop conditions are met.

Although the above algorithm is independent of the actual number of targets, it may erroneously identify spurious values as targets. To mitigate this issue, in Sec. IV we will propose a clustering-based strategy designed to merge multiple detections that likely correspond to the same physical target.

III. Experimental Testbed for 5G-compliant ISAC

The main components of the developed experimental testbed are depicted at the bottom of Fig. 2. A Linux-based workstation governs the entire setup, hosting the software stack described in Sec. III-A, and interfacing with two Software Defined Radio (SDR) units (NI Ettus USRP X410, with a maximum transmission power of $23\,\text{dBm}$) via a $4\times$SFP28-to-QSFP28 connection. These SDRs serve as the RF front-ends for both the gNB and the UE. The spatial constraints imposed by the laboratory dimensions, together with the power limitations of the SDR hardware — resulting in target reflections that are too weak to be reliably detected — make it impractical to experiment with long distances or high-speed moving reflectors. To overcome this limitation, a Keysight PROPSIM FS16 channel emulator is integrated into the setup, enabling a realistic emulation of an outdoor scenario with both static and moving scatterers and allowing a controlled evaluation of the sensing performance. Physical links between the SDRs and the channel emulator, as well as internal architecture, are detailed in Sec. III-B.

A. 5G-compliant ISAC Framework

As shown in Fig. 2, the proposed ISAC framework implements the full stack of the 5G standard, hence adhering to the communications-centric design (reuse of an existing communication system). It comprises the *Communication Subsystem* and the *Sensing Subsystem*. The former is based on OAI, an open-source implementation of the 5G protocol stack, used to realize a 5G Core Network (CN) and two endpoints of the Radio Access Network (RAN), namely the UE and the gNB. Note that, even in the presence of the gNB alone (no traffic channels), sensing remains feasible through the

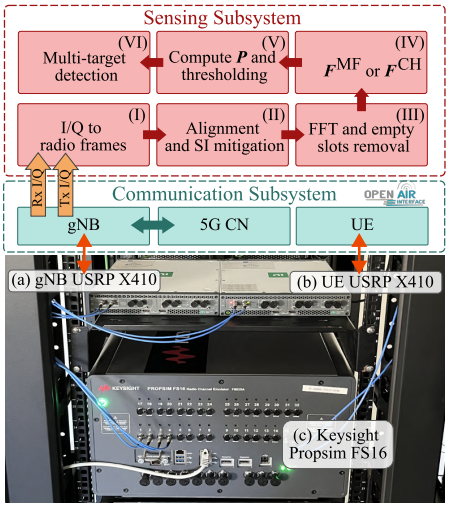

Fig. 2. Scheme of the main components and picture of the experimental testbed for 5G-compliant downlink ISAC.

always-on (control) signals described in Sec. II-A. Additional details on the 5G CN and UE, as well as the commands used to launch the gNB node for low-level data logging can be found in [12]. The I/Q samples at the gNB are passed to the Sensing Subsystem for processing through a C++/MATLAB pipeline: (I) TX and RX I/Q samples are arranged into a single radio frame of 10 ms; (II) these are temporally aligned to compensate for software and hardware processing delays, and SI is estimated and mitigated; (III) $\boldsymbol{X}$ and $\tilde{\boldsymbol{Y}}$ are obtained by removing the CP and computing the Fast Fourier Transform (FFT) of the active slots; (IV) $\boldsymbol{F}^{\text{MF}}$ or $\boldsymbol{F}^{\text{CH}}$ is computed; (V) range–Doppler map $\boldsymbol{P}$ is then computed via (1); and (VI) the multi-target detection algorithm in II-C is employed to identify and estimate range and velocity of the dominant scatterers.

B. Multipath Channel Emulation

The Keysight PROPSIM FS16 channel emulator used in our experimental testbed can apply channel effects to the signals entering an IN port and return them through a corresponding OUT port. The overall physical and logical (emulated) connections between the gNB and UE SDRs are depicted in Fig. 3. Even-numbered ports act as IN, whereas odd-numbered ports are OUT. On the physical connection side (shown in blue), the TX and RX channels of the gNB SDR are connected to emulator ports 2 and 1, respectively, while the UE SDR is linked via RF cables to ports 4 and 3. Regarding the emulation logic, two operational modes are available: *Cellular Systems* and *MANET*. The former allows for the definition of a set of access points and user devices, enabling the configuration of specific channel models between them. Conversely, the *MANET* mode enables the emulation of a mesh network in which signals transmitted from the TX port of a device are propagated (after being altered by the emulator) to the RX ports of all other devices, without assigning specific node roles. Since the emulation of a multipath (scattering) environment requires that a device's transmitted signal also reach its own RX channel, the MANET mode has been

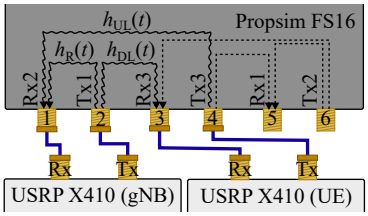

Fig. 3. Connections between SDRs and the Keysight PROPSIM FS16 channel emulator, with the emulated channels between the RF IN/OUT ports.

adopted to define three virtual full-duplex devices. Device 1 (Tx1/Rx1) and Device 2 (Tx2/Rx2) are used as the TX and RX channel of the gNB, respectively. Specifically, the gNB transmissions enter port 2 (Tx1) and, after the application of the channel models corresponding to the downlink ($h_{\text{DL}}(t)$) and the reflected link ($h_{\text{R}}(t)$), exit through ports 1 (Rx2, i.e., the gNB RX channel) and 3 (Rx3, i.e., the RX channel of the UE), respectively. Conversely, the UE TX signals enter port 4 (Tx3) and exit through port 1 after being modified according to the uplink channel $h_{\text{UL}}(t)$. Ports 5 and 6 remain unused, although they are assigned to the virtual channels Rx1 and Tx2.

The channel models associated with the communication links (either uplink or downlink) between the gNB and the UE, which we recall are not relevant to the ISAC operations, are modeled as single-path flat-fading channels $h_{\text{DL}}(t) = h_{\text{UL}}(t) = \alpha_{\text{comm}}\delta(t-\tau_{\text{comm}})$, where α_{comm} denotes the complex path gain (accounting for path loss, phase, and any static shadowing) and τ_{comm} is the propagation delay of the communication link. The backscatter signal captured at the gNB RX channel for ISAC purposes, consisting of the SI and the replicas originated from surrounding scatterers, is modeled as a classical multipath channel with impulse response given by

$$h_{\text{R}}(t) = \alpha^{\text{SI}}\delta(t-\tau^{\text{SI}}) + \sum_{i=1}^{N_{\text{scat}}} \alpha_i e^{j2\pi f_i t}\,\delta(t-\tau_i), \qquad (7)$$

where α^{SI} and τ^{SI} are the attenuation factor and delay of the direct link between the TX and RX channels, i.e., the SI component. The parameters α_i, f_i, and τ_i represent the attenuation factor, Doppler frequency shift, and propagation delay of the i-th scatterer, respectively. Specifically, α_i is computed according to the well-know radar equation. Model (7) is implemented by means of the PROPSIM Aerospace and Satellite Modelling Tool (ASO), which enables the definition of a Doppler shift characterizing each path. It is worth noting that when ASO is employed, a non-negligible insertion delay is introduced on the RF links. The latter is compensated by running the OAI nodes with the `-A` parameter specifying the delay in samples.

IV. Experimental Results

For our experimental campaign with the testbed of Sec. III, we set $f_{\text{carrier}} = 3.995$ GHz, which lies within the n77 band (FR1, sub-6 GHz), $\Delta f = 30$ kHz and maximum bandwidth of $B = 100$ MHz, corresponding to $N_{\text{RB}} = 273$ RBs (i.e., $S = 3276$ subcarriers). For ISAC, as mentioned in Sec. I, we process a *single radio frame* (of 10 ms), which contains

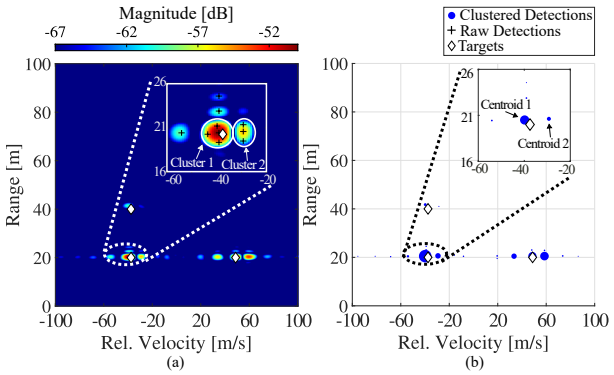

Fig. 4. (a) Range-Doppler map, (b) multi-target detection with clustering results, using communication (data payload) signals.

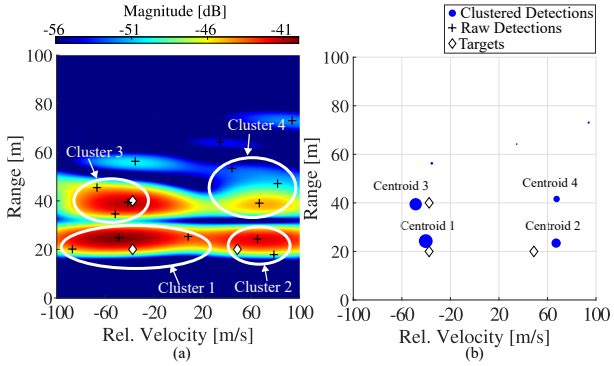

Fig. 5. (a) Range-Doppler map, (b) multi-target detection with clustering results, using always-on (control) signals with *SIB_tda*=5.

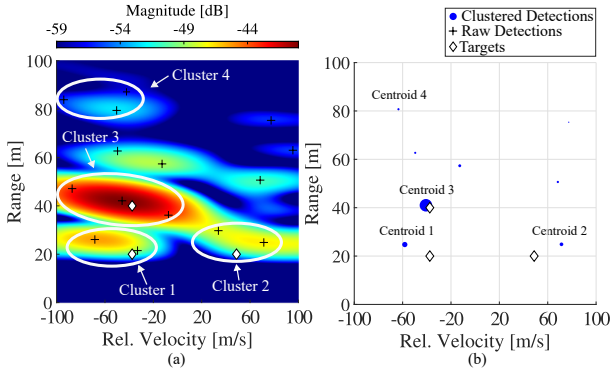

Fig. 6. (a) Range-Doppler map, (b) multi-target detection with clustering results, using always-on (control) signals with *SIB_tda*=1.

$M = 280$ OFDM symbols; this will reveal the lower bound of practically achievable performance. All I/Q samples were captured at a sampling frequency $f_{\text{samp}} = 122.88\,\text{MHz}$. For the SI mitigation algorithm, the same parameters adopted in [12] are used. The range-Doppler maps $\boldsymbol{P}$ are computed using $\tilde{S} = 10S$ and $\tilde{M} = 5M$. Regarding the processing strategy, we adopt the $\boldsymbol{F}^{\text{CH}}$ approach when using communication signals, as the latter occupy the entire bandwidth without spectral gaps. Indeed, $\boldsymbol{F}^{\text{CH}}$ produces lower (range profile) sidelobes in the range-Doppler maps compared to $\boldsymbol{F}^{\text{MF}}$, leading to improved performance in the multi-target scenarios [19]. Conversely, as discussed in Sec. II-A (and illustrated in Fig. 1), the always-on control signals occupy more limited time-frequency resources. Under these conditions, the $\boldsymbol{F}^{\text{CH}}$ approach would suffer from numerical instabilities when processing inactive subcarriers (owing to divisions by values close to zero), so making $\boldsymbol{F}^{\text{MF}}$ preferable. We generate through the channel emulator $N_{\text{scat}} = 3$ targets, each with a specific distance R_i and relative velocity V_i, $i = 1, \ldots, N_{\text{scat}}$. In particular, $R_1 = R_3 = 20\,\text{m}$ and $R_2 = 40\,\text{m}$, while $V_1 = V_2 = -37.5\,\text{m/s}$ and $V_3 = 48.8\,\text{m/s}$. From such values, the corresponding delays τ_i and Doppler shifts f_i are obtained. Regarding α^{SI}, it is set such that the PROPSIM output power of the emulated SI channel is $-23\,\text{dBm}$, i.e., the maximum supported value. With regard to α_1, α_2 and α_3, are set as to experiment a path-loss of $26\,\text{dB}$, $31\,\text{dB}$ and $26\,\text{dB}$ higher than SI, respectively. Such values are computed via the radar equation considering a $30\,\text{dBi}$ antenna gain and a Radar Cross-Section (RCS) of $10\,\text{m}^2$.

As to the multi-target detection algorithm, to compute η we need to empirically estimate F_z from $\boldsymbol{P}$. To this aim, we consider a set of cells that lie in the upper region of $\boldsymbol{P}$, beyond a given range index r_{max}. This range index can be selected based on the maximum detectable distance $R_{\text{max}} = \frac{cT_{\text{CP}}}{2}$, where T_{CP} is the CP duration [11], such that no useful targets can appear beyond it, i.e., we safely select cells where only noise is present. From (2), we have that $r_{\text{max}} = \frac{2\tilde{S}\Delta f R_{\text{max}}}{c}$. To obtain an empirical CDF $\hat{F}_z$, we thus consider a region including $Q = 5000$ rows of $\boldsymbol{P}$, from r_{max} to $r_{\text{max}} + Q - 1$. Then, we fix a $P_{\text{fa}} = 10^{-3}$ and compute η using $\hat{F}_z$ in (6).

As anticipated at the end of Sec. II-C, the multi-target detection algorithm yields a list of candidate raw detections that must be further processed to discard those belonging to the same lobes of the range–Doppler map, as they likely identify the same physical target. To this end, we propose a clustering strategy that starts by selecting the cell (r, v) with the maximum magnitude in the list. We then test which of the remaining candidate detections in the list are connected to it through segments that traverse cells of the range–Doppler map whose magnitudes exhibit a monotonically decreasing trend. Candidates satisfying this condition, obtained through Bresenham's line computation, are grouped into the same cluster, as they belong to the same dominant lobe. The cluster centroid is then computed as an amplitude-weighted mean of the selected points, which are then removed from the list and the process is repeated until all the detections are assigned to clusters. The final centroids characterize the distance and velocity of the detected targets. Note that a direct comparison with other well-known clustering algorithms (e.g., K-means, DBSCAN) would not be possible, as the proposed method exploits information from the range-Doppler map.

A. ISAC with Communication Signals

Once the UE is connected to our 5G network, we initiate a downlink data transmission using the *iperf3* utility. The analyzed frame contains $S_{\text{act}} = 3276$ active subcarriers and $M_{\text{act}} = 156$, (a detailed description of this type of signals is reported in [12]). Fig. 4(a) shows the resulting range–Doppler

map (using $\boldsymbol{F}^{\mathrm{CH}}$) with white diamonds representing the actual targets and black crosses the raw detections, while Fig. 4(b) reports the corresponding outputs of the multi-target detection algorithm with proposed clustering procedure. The radius of the blue dots is proportional to the magnitude of the detected targets. The comparison of the two figures shows that the algorithm successfully identifies the true targets' ranges and velocities. While multiple spurious values are erroneously identified as targets in the raw detections, resulting in false alarms, the additional clustering step can effectively merge them into a single (clustered) detection.

B. ISAC with Always-on Signals

We considered two configurations of always-on signals periodically transmitted by the gNB, namely *SIB_tda*=1 and *SIB_tda*=5, which produce two different allocations of the SIB1 block (see Sec. II-A). Fig. 5(a) shows the range–Doppler map (using $\boldsymbol{F}^{\mathrm{MF}}$) for *SIB_tda*=5. Also in this case, the multi-target detector with proposed clustering can effectively groups raw detections belonging to the same lobes in the range-Doppler map. Overall, sensing performance is visibly worse than the communication case of Fig. 4 due to the much reduced number of symbols and subcarriers — $S_{\mathrm{act}}^{\mathrm{tda=5}} = 559, M_{\mathrm{act}}^{\mathrm{tda=5}} = 12$, which amounts to only 17% of the active subcarriers and 8% of the OFDM symbols used by the communication signals. This directly affects both the overall resolution and widens the beamwidth of both mainlobe and sidelobes. In spite of that, Fig. 5(b) reveals that the delivered estimation accuracy of ranges and Doppler shifts for the three targets is satisfactory.

Fig. 6(a) finally shows the case *SIB_tda*=1. In this configuration, the number of subcarriers is further reduced ($S_{\mathrm{act}}^{\mathrm{tda=1}} = 438$, whereas $M_{\mathrm{act}}^{\mathrm{tda=1}} = 14$). This has a detrimental effect on performance in terms of range estimation. As shown in Fig. 6(b), the number of false alarms generated by sidelobes and residuals is higher than in the *SIB_tda*=5 case (Fig. 5(b)).

V. Conclusion

We investigated downlink monostatic ISAC using a full-stack 5G-compliant testbed, enabling the evaluation of sensing performance in complex scattering environments. A fully digital processing pipeline is developed, comprising temporal alignment of TX/RX I/Q samples, SI mitigation, and matched-filter or channel-estimation-like processing to generate range-Doppler maps. A multi-target detection algorithm was then implemented, followed by a novel clustering strategy to mitigate the false alarms arising from redundant raw detections. We compared the use of communication and always-on control signals. Experimental results confirm superior performance of communication signals, but also reveal that specific always-on configurations can still deliver useful and persistent sensing information for ISAC.

Acknowledgements

This work was supported by the EU under Italy NRRP (NextGenerationEU): RESTART (PE00000001, CUP: D93C22000910001), MOST (CN00000023, CUP: D93C22000410001), and SERICS (PE00000007, CUP: D33C22001300002, project ISP5G+). Additional support came from PRIN 2022 projects INSPIRE (2022BEXMXN 01) and HORUS (2022P44KA8) funded by MUR, and the HORIZON MSCA project BRIDGITISE (grant 101119554).

References

[1] N. González-Prelcic, D. Tagliaferri, M. F. Keskin, H. Wymeersch, and L. Song, "Six Integration Avenues for ISAC in 6G and Beyond," *IEEE Vehicular Technology Magazine*, vol. 20, no. 1, pp. 18–39, 2025.

[2] X. Li, Y. Cui, J. A. Zhang, F. Liu, D. Zhang, and L. Hanzo, "Integrated Human Activity Sensing and Communications," *IEEE Communications Magazine*, vol. 61, no. 5, pp. 90–96, 2023.

[3] A. Liu, Z. Huang, M. Li, Y. Wan, W. Li, T. X. Han, C. Liu, R. Du, D. K. P. Tan, J. Lu, Y. Shen, F. Colone, and K. Chetty, "A Survey on Fundamental Limits of Integrated Sensing and Communication," *IEEE Comm. Surveys & Tutorials*, vol. 24, no. 2, pp. 994–1034, 2022.

[4] A. Fascista, A. De Monte, A. Coluccia, H. Wymeersch, and G. Seco-Granados, "Low-Complexity Downlink Channel Estimation in mmWave Multiple-Input Single-Output Systems," *IEEE Wireless Communications Letters*, vol. 11, no. 3, pp. 518–522, 2022.

[5] A. Coluccia and A. Fascista, "Low-Complexity Prediction of Energy Statistic Exceedance Probability for η-μ Variates," *IEEE Signal Processing Letters*, vol. 31, pp. 3094–3098, 2024.

[6] F. Liu, Y.-F. Liu, Y. Cui, C. Masouros, J. Xu, T. X. Han, S. Buzzi, Y. C. Eldar, and S. Jin, "Sensing With Communication Signals: From Information Theory to Signal Processing," *IEEE Journal on Selected Areas in Communications*, pp. 1–1, 2025.

[7] N. Maletic, M. Petri, M. Appel, and E. Grass, "A Software-Defined Radio Solution for Integrated mmWave Communication and Sensing," in *2025 IEEE Wireless Communications and Networking Conference (WCNC)*. IEEE, 2025, pp. 1–6.

[8] B. Duan, T. Li, W. Pan, H. Zhou, Y. Shen, Y. Liu, and S. Shao, "In-Band Full-Duplex Communication for OFDM Integrated Sensing and Communication Systems," *IEEE Internet of Things Journal*, 2025.

[9] M. Yazgan, H. Arslan, and S. Vakalis, "High-Accuracy Indoor Ranging Using Microwave OFDM Signals," *IEEE Microwave and Wireless Technology Letters*, vol. 34, no. 12, pp. 1407–1410, 2024.

[10] S. Ding, B. Chen, J. Li, J. Yao, Y. Yuan, D. Jiang, and F. Qin, "Integrated Sensing and Communication: Prototype and Key Processing Algorithms," in *2023 IEEE International Conference on Communications Workshops (ICC Workshops)*, 2023, pp. 225–230.

[11] C. Baquero Barneto, T. Riihonen, M. Turunen, L. Anttila, M. Fleischer, K. Stadius, J. Ryynänen, and M. Valkama, "Full-Duplex OFDM Radar With LTE and 5G NR Waveforms: Challenges, Solutions, and Measurements," *IEEE Transactions on Microwave Theory and Techniques*, vol. 67, no. 10, pp. 4042–4054, 2019.

[12] S. Carbonara, D. Pugliese, A. Fascista, A. Coluccia, and G. Boggia, "5G-Compliant Integrated Sensing and Communication at Sub-6 GHz: Experiments with SDRs and OpenAirInterface," in *European Wireless 2025; 30th European Wireless Conference*, Sophia Antipolis, France, 2025. [Online]. Available: https://telematics.poliba.it/wp-content/uploads/publications/2025/EW25Carbonara.pdf

[13] M. Golzadeh, E. Tiirola, L. Anttila, J. Talvitie, K. Hooli, O. Tervo, I. Peruga, S. Hakola, and M. Valkama, "Downlink Sensing in 5G-Advanced and 6G:SIB1-assisted SSB Approach," in *2023 IEEE 97th Vehicular Technology Conference (VTC2023-Spring)*, 2023, pp. 1–7.

[14] J. Kim and N. Lee, "Adaptive Non-Linear Digital Self-Interference Cancellation for Full-Duplex Wireless Systems Using Ito-Hermite Polynomials," in *2018 ICC Workshops*, 2018, pp. 1–6.

[15] M. F. Keskin, M. M. Mojahedian, J. O. Lacruz, C. Marcus, O. Eriksson, A. Giorgetti, J. Widmer, and H. Wymeersch, "Fundamental Trade-Offs in Monostatic ISAC: A Holistic Investigation Towards 6G," *IEEE Transactions on Wireless Communications*, pp. 1–1, 2025.

[16] M. Braun, C. Sturm, and F. K. Jondral, "Maximum likelihood speed and distance estimation for OFDM radar," in *2010 IEEE Radar Conference*, 2010, pp. 256–261.

[17] M. A. Richards, J. A. Scheer, and W. A. Holm, Eds., *Principles of Modern Radar: Basic Principles*. Raleigh, NC, USA: SciTech Publishing, 2010.

[18] M. Braun, M. Fuhr, and F. K. Jondral, "Spectral Estimation-Based OFDM Radar Algorithms for IEEE 802.11a Signals," in *2012 IEEE Vehicular Technology Conference (VTC Fall)*, 2012, pp. 1–5.

[19] C. Sturm and W. Wiesbeck, "Waveform Design and Signal Processing Aspects for Fusion of Wireless Communications and Radar Sensing," *Proceedings of the IEEE*, vol. 99, no. 7, pp. 1236–1259, 2011.